



Article

Effects of Addition of Cu_xO to Porous SnO_2 Microspheres Prepared by Ultrasonic Spray Pyrolysis on Sensing Properties to Volatile Organic Compounds

Soichiro Torai, Taro Ueda , Kai Kamada, Takeo Hyodo  and Yasuhiro Shimizu *

Graduate School of Engineering, Nagasaki University, 1-14 Bunkyo-Machi, Nagasaki 852-8521, Japan

* Correspondence: shimizu@nagasaki-u.ac.jp

Abstract: Porous (pr-) SnO_2 -based powders were synthesized by ultrasonic spray pyrolysis employing home-made polymethylmethacrylate (PMMA) microspheres (typical particle size: 70 nm in diameter), and effects of the Cu_xO addition to the pr- SnO_2 powder on the acetone and toluene sensing properties were investigated. Well-developed spherical pores reflecting the morphology of the PMMA microsphere templates were formed in the SnO_2 -based powders, which were quite effective in enhancing the acetone and toluene responses. The 0.8 wt% Cu-added pr- SnO_2 sensor showed the largest acetone response at 350 °C among all the sensors. Furthermore, we clarified that the addition of Cu_xO onto the pr- SnO_2 decreased the concentration of carrier electrons and the acetone-oxidation activity, leading to the improvement of the acetone-sensing properties of the pr- SnO_2 sensor.

Keywords: semiconductor gas sensor; tin oxide; copper; ultrasonic spray pyrolysis; polymethylmethacrylate; acetone; toluene



Citation: Torai, S.; Ueda, T.; Kamada, K.; Hyodo, T.; Shimizu, Y. Effects of Addition of Cu_xO to Porous SnO_2 Microspheres Prepared by Ultrasonic Spray Pyrolysis on Sensing Properties to Volatile Organic Compounds. *Chemosensors* **2023**, *11*, 59. <https://doi.org/10.3390/chemosensors11010059>

Academic Editors: Elisabetta Comini and Ana Rovisco

Received: 19 December 2022

Revised: 5 January 2023

Accepted: 9 January 2023

Published: 11 January 2023



Copyright: © 2023 by the authors. Licensee MDPI, Basel, Switzerland. This article is an open access article distributed under the terms and conditions of the Creative Commons Attribution (CC BY) license (<https://creativecommons.org/licenses/by/4.0/>).

1. Introduction

Volatile organic compounds (VOCs) are emitted from factories, automobiles, adhesives, paints, etc., and they are known to be harmful to the human body even at low concentrations [1–3]. In addition, the exhaled breath of patients contains a higher concentration of specific VOCs or volatile sulfide compounds (VSCs) than that of healthy people. For example, patients suffering from lung cancer and diabetes are known to release high concentrations of toluene and acetone, respectively [4–10]. The establishment of highly sensitive and selective gas-sensing systems effectively prevents the VOC exposure in the living environment as well as sufficiently contributes to the realization of sophisticated non-invasive diagnostic methods for lung cancer and diabetes in the near future. Therefore, compact, inexpensive, and lightweight gas sensors were actively developed by various research and development organizations. Among them, semiconductor-type gas sensors employing metal oxides have been used as gas-leak detectors for the detection of reducing gases such as CO and hydrocarbons. The sensing mechanism of the semiconductor-type gas sensors is based on the change in electrical resistance of the sensing materials, mainly n-type semiconductors (e.g., SnO_2 , WO_3 , and In_2O_3), upon exposure to target gases. Oxygen molecules exist as negatively adsorbed oxygen species (O^- and/or O^{2-} at elevated temperatures) on the metal-oxide surface, and they trap a certain number of free electrons from the conduction band of the metal oxide. These oxygen adsorbates react with reducing gases, and then trapped electrons go back to the conduction band of the metal oxide, which results in a decrease in the sensor resistance. A comparable amount of the reducing gases are oxidized and consumed in the process of gas diffusion from the top of the thick film sensor to the vicinity of the interdigitated electrodes located at the innermost portion of the thick film sensor. Therefore, the structural controls of mesopores as well as macropores of the semiconducting metal oxides is of great importance to improve the gas diffusivity,

gas-adsorption properties, and catalytic combustion behavior of the reducing gases. Therefore, our group has focused on the precise control of the microstructural morphology of various gas-sensing materials during the last 20 years. For example, we have synthesized mesoporous and macroporous oxides by utilizing the assembly of surfactants with a size of several nanometers and commercial polymethylmethacrylate (PMMA) microspheres with a diameter of more than 150 nm, respectively, and the introduction of such well-developed porous structures into the sensor materials improved their response properties to various gases [11]. Recently, we have also synthesized the middle-sized PMMA microspheres (10–100 nm in diameter) as a template for middle-sized pores by ultrasonic-assisted polymerization, and we have succeeded in developing spherical metal-oxide powders (SnO_2 and In_2O_3) with well-developed middle-sized pores by ultrasonic-spray pyrolysis employing these PMMA microspheres as a template. The semiconductor-type gas sensors fabricated with their porous SnO_2 and In_2O_3 powders exhibited very large responses to H_2 and NO_2 , respectively [12–14]. In addition, we have also demonstrated that the Au loading on the porous In_2O_3 (pr- In_2O_3) powder was effective in enhancing the NO_2 response [15–17].

Generally, n-type semiconductors such as SnO_2 and WO_3 are common gas-sensitive materials. For further improvement of their gas sensing properties, the loading with various materials on the surface (e.g., noble metals or p-type semiconductors) has been reported in the past couple of decades. The loading with noble-metal nanoparticles such as Au or Pt effectively enhances their VOC-sensing properties [18–22]. However, the excessive utilization of noble metals hinders the sensor devices from cost-effective fabrication. On the other hand, it is also well known that the loading of p-type metal oxides on the surface of n-type metal oxides and thus the forming of p–n heterojunctions between them are quite effective in improving the gas-sensing properties [23–30]. Jayababu et al. reported that the NiO-loaded SnO_2 sensor showed a larger response to ethanol than the SnO_2 or NiO sensor, and an increase in the thickness of the depletion layer at the p–n heterojunction was interpreted as a possible reason for the enhanced sensor responses [25]. Cai et al. successfully synthesized the SnO_2 nanowires loaded with and without Cr_2O_3 nanoparticles, and they clarified that the p–n heterojunctions formed on the nanowire surface improved the ethanol response [26]. Namely, the forming of p–n heterojunctions is one important technique in improving the gas-sensing properties. Furthermore, the control of catalytic activities of the gas-sensing materials for the oxidation of the target gas is one very important factor in improving their sensor responses [31–33].

In this study, porous (pr-) SnO_2 and Cu_xO -added pr- SnO_2 powders were synthesized by ultrasonic spray pyrolysis employing homemade PMMA microspheres (typical particle size: 70 nm in diameter), and their acetone and toluene sensing properties were examined. We also evaluated changes in resistance between dry nitrogen and dry synthetic air (21% O_2) as well as catalytic activities of acetone and toluene oxidation by the addition of Cu_xO . Based on the results obtained, the effects of the addition of Cu_xO on the improved acetone response of the sensors are discussed.

2. Materials and Methods

2.1. Preparation of Pr- SnO_2 Powders

Porous (pr-) SnO_2 and Cu_xO -added pr- SnO_2 powders were synthesized by ultrasonic spray pyrolysis employing homemade PMMA microspheres as a template in a similar manner reported previously [12–14,17,23,34,35]. The typical particle size of the PMMA microspheres used was ca. 70 nm. A precursor solution was prepared by mixing the PMMA microspheres (0.32 g dm^{-3} , 40 mL) with SnCl_4 aqueous solution (0.05 mol dm^{-3} , 60 mL). An appropriate amount of CuCl_2 aqueous solution (0.05 mol dm^{-3}) was also prepared in order to add Cu_xO to pr- SnO_2 . The prepared solution was atomized by ultrasonication, and it was introduced into an electric furnace at $1100 \text{ }^\circ\text{C}$ under flowing air ($1500 \text{ cm}^3 \text{ min}^{-1}$). After the evaporation of water and the thermal decomposition of SnCl_4 , CuCl_2 , and PMMA microspheres, spherical porous SnO_2 powder was produced in the electric furnace, and

Cu_xO nanoparticles were highly dispersed in the SnO_2 powder. The obtained pr- SnO_2 powders added with and without Cu_xO were denoted as pr- $w\text{Cu-SnO}_2$ and pr- SnO_2 [w : the additive amount of Cu (wt%), $w = 0.4, 0.8, 1.6$], respectively. For comparative purposes, a spherical dense SnO_2 (d- SnO_2) powder was also prepared by a similar preparation technique using the precursor solution without containing PMMA microspheres.

2.2. Sensor Fabrication and Gas Sensing Measurements

The SnO_2 -based powder was mixed with α -terpineol at a weight ratio of 1:2 to make a paste, and the paste was screen printed onto an alumina substrate equipped with a pair of interdigitated Pt electrodes (gap size: ca. 200 μm), followed by drying at 100 $^\circ\text{C}$. Then, they are calcined at 550 $^\circ\text{C}$ for 5 h in ambient air. Figure 1 shows a schematic drawing of the sensor element. Gas responses of these sensors to 20, 50, and 100 ppm VOCs (acetone and toluene) balanced with dry air were measured using a conventional gas-flow apparatus equipped with a furnace in an operating temperature of 300–500 $^\circ\text{C}$. The total flow rate was fixed at 100 $\text{cm}^3 \text{min}^{-1}$. The resistance of the sensors was directly measured by using a data acquisition system (Keysight Technologies, Inc., Santa Rosa, CA, USA, DAQ 970A). The magnitude of response to VOCs was defined as the ratio (R_a/R_g), where R_g and R_a are the resistance in VOCs balanced with air and that in air.

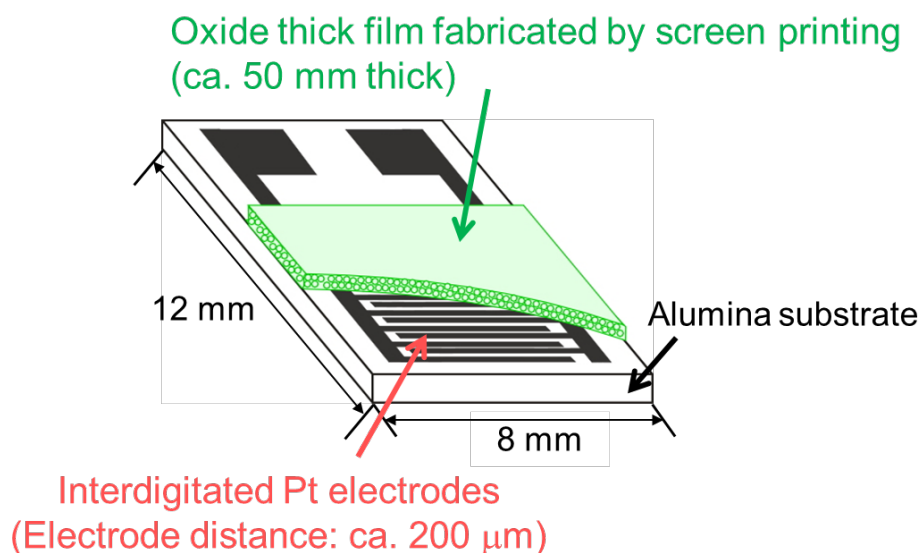


Figure 1. Schematic drawing of a sensor element.

2.3. Characterization

Scanning electron microscopy (SEM) images of synthesized powders were collected by using an electron microscope (JEOL Ltd., Tokyo, Japan, JSM-7500F). The more detailed structure of these powders was observed by transmission electron microscopy (TEM; JEOL Ltd., JEM-ARM200F) and scanning transmission electron microscopy with energy dispersive X-ray spectroscopy for elemental mapping (STEM-EDS; JEOL Ltd., JEM-ARM200F). N_2 adsorption-desorption isotherms were recorded, and the pore-size distribution and specific surface area (SSA) of these powders were calculated by using Barrett–Joyner–Halenda (BJH) and Brunauer–Emmett–Teller (BET) methods, respectively (Micromeritics Instrument Corp., Norcross, GA, USA, Tristar3000). The phase and crystal structure of these powders were confirmed by X-ray diffraction analysis (XRD; Rigaku Corp., Tokyo, Japan, Miniflex600-DX) using $\text{Cu K}\alpha$ radiation (40 kV, 40 mA), and their crystallite size (CS) was calculated by utilizing the Scherrer equation (shaper factor: 0.9). Chemical state of the surface of these powders was characterized by X-ray photoelectron spectroscopy using $\text{Al K}\alpha$ radiation (XPS, Kratos Analytical Ltd., Manchester, UK, Axis Ultra DLD).

2.4. Catalytic Combustion Activity

Granules of the pr-SnO₂ or pr-1.6Cu-SnO₂ (ca. 20–60 mesh) were prepared by a press of the powders into discs and crushed. The granules of about 0.05 g were fixed in a glass reactor connected to a flow apparatus. They were exposed to 100 ppm acetone balanced with dry air, at a flow rate of 30 cm³ min⁻¹ (a gas hourly space velocity (GHSV) of 12,732 h⁻¹). The pr-SnO₂ or the pr-1.6Cu-SnO₂ powder was heated in the temperature range of 30–500 °C, and the outlet gas was characterized by using a gas chromatograph/mass spectroscope (GC-MS; Shimadzu Corp., Kyoto, Japan, GCMS-QP2010SE with a capillary column, PoraPLOT Q) and a GC equipped with an FID detector (Shimadzu Corp., Kyoto, Japan, GC-2010 with a capillary column, DB-5)).

3. Results and Discussion

3.1. Crystal Structure and Morphology of the Powder

Figure 2 shows SEM photographs of representative as-prepared d-SnO₂, pr-SnO₂, and pr-*w*Cu-SnO₂ (*w*: 0.4, 0.8, 1.6) powders, together with the particle-size distributions of their powders obtained by counting 50 particles in their SEM images. The obtained powders were almost spherical with diameters of 100–900 nm, which were widely distributed depending on the size of the precursor mists which were fed into the electric furnace [16]. The pores were hardly formed on the surface of the d-SnO₂ powder. On the other hand, the well-developed pores were structured on the surface of the pr-SnO₂ and pr-*w*Cu-SnO₂ powders, because they originated from the thermal decomposition of the PMMA microspheres added into the precursor solution subjected to the ultrasonic spray pyrolysis. Their morphologies and particle sizes were almost independent of the amounts of Cu_xO added.

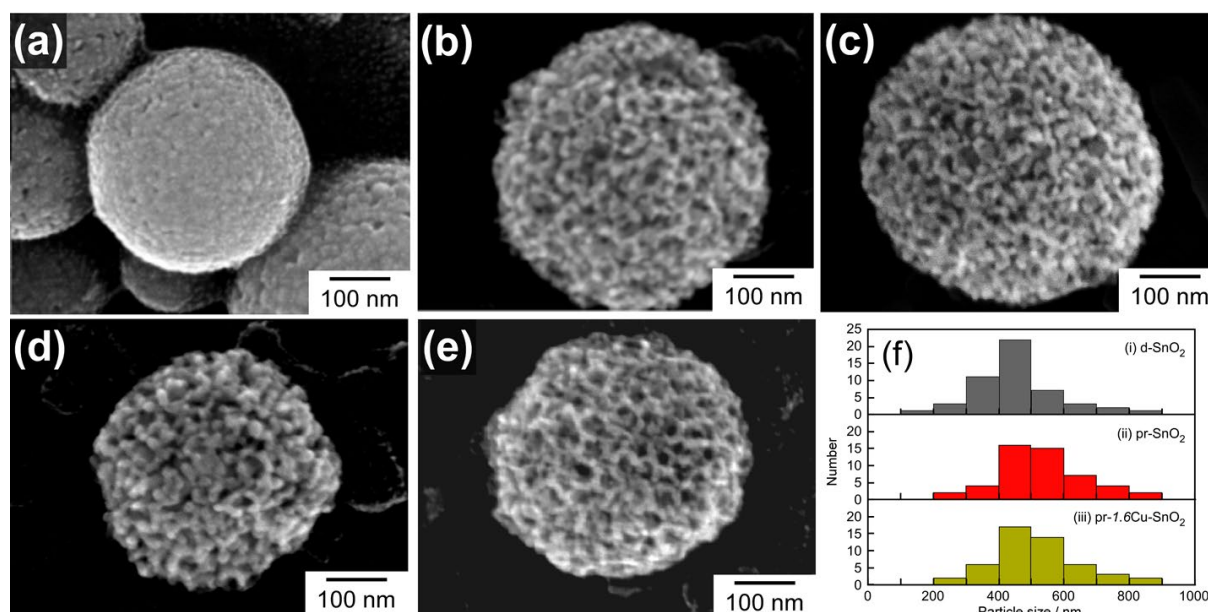


Figure 2. SEM photographs of as-prepared (a) d-SnO₂, (b) pr-SnO₂, and representative pr-*w*Cu-SnO₂ (*w*: (c) 0.4, (d) 0.8, (e) 1.6) powders, together with (f) their particle-size distributions obtained by counting of 50 particles in their SEM images.

Figure 3 shows TEM photographs of as-prepared pr-SnO₂ and pr-1.6Cu-SnO₂ powders. It is confirmed that the porous structure was well developed even in the internal region of these spherical powders (Figure 3(ai,bi)). The TEM images showed that the size of SnO₂ polycrystals was ca. 10–30 nm in diameter (Figure 3(aii,bii)). The elemental mapping of the pr-1.6Cu-SnO₂ powder by using STEM-EDS showed uniform dispersion of Cu components in the prepared powder as shown in Figure 3(biii,iv). The amount of Cu added to the pr-1.6Cu-SnO₂ powder, which was measured by EDS, was ca. 1.88 wt%.

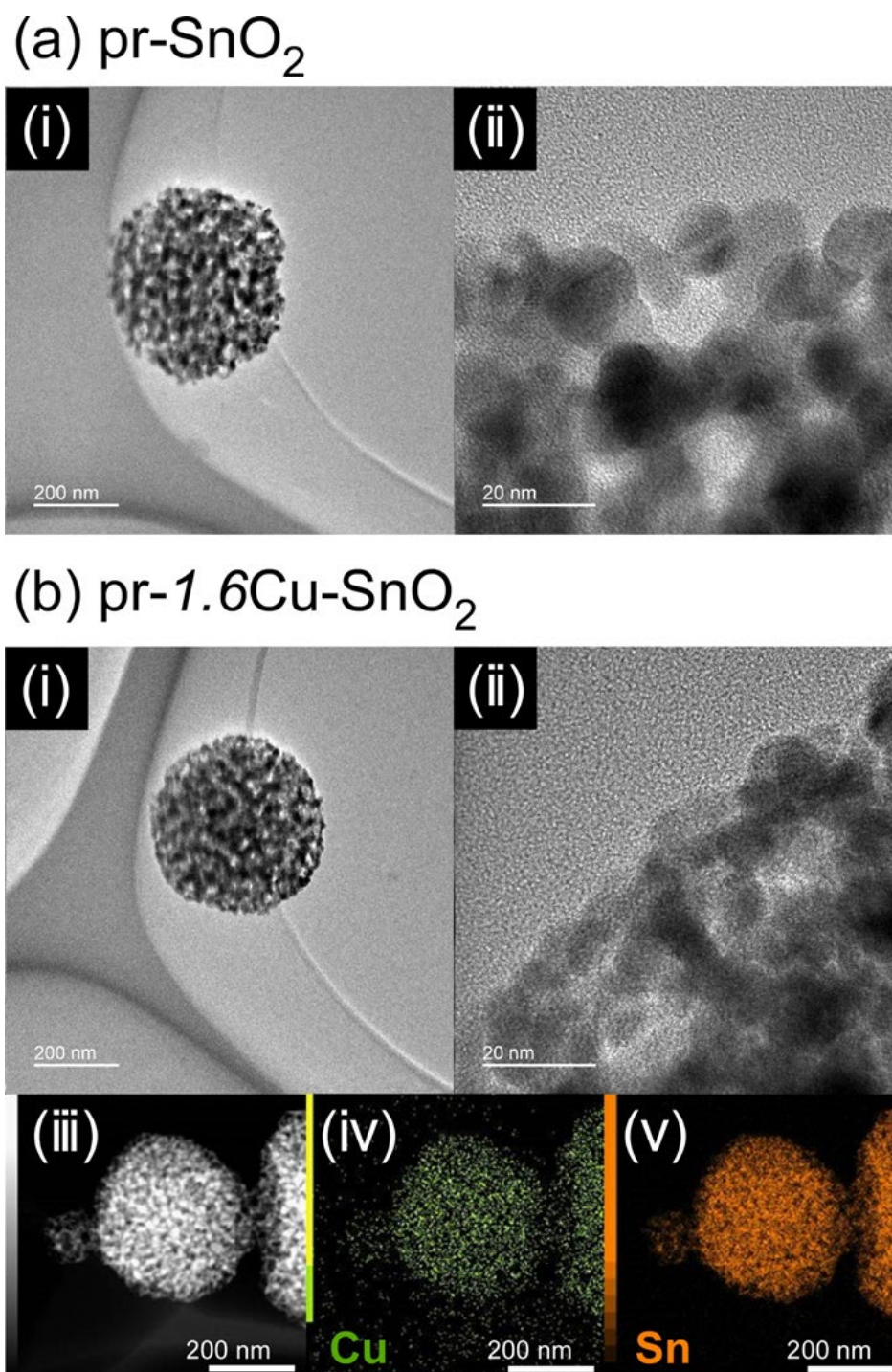


Figure 3. TEM photographs of as-prepared (a) (i,ii) pr-SnO₂ and (b) (i,ii) pr-1.6Cu-SnO₂ powders. STEM photograph of as-prepared pr-1.6Cu-SnO₂ powders ((b) (iii)) and their EDS elemental mappings ((b) (iv): Cu and (b) (v): Sn).

Figure 4 shows XRD patterns of d-SnO₂, pr-SnO₂, and pr-*w*Cu-SnO₂ (*w*: 0.4, 0.8, 1.6) powders. All powders exhibited three large peaks corresponding to the (110), (101), and (211) planes of the cassiterite-type structure (JCPDF No. 00-021-1250). In addition, no diffraction patterns of Cu_xO were observed in these XRD spectra. The crystallite size of pr-SnO₂ (ca. 8.65 nm) was smaller than that of d-SnO₂ (ca. 20.3 nm), due to the formation of the porous SnO₂ structure via the decomposition of PMMA template [12–14,17,23,34,35]. In contrast, the small amount of Cu_xO addition (0.4 wt%) caused a slight increase in the

crystallite size from ca. 8.65 nm to ca. 8.88 nm, whereas the further increase in the Cu content tended to decrease the crystallite size (e.g., ca. 7.08 nm for pr-1.6Cu-SnO₂).

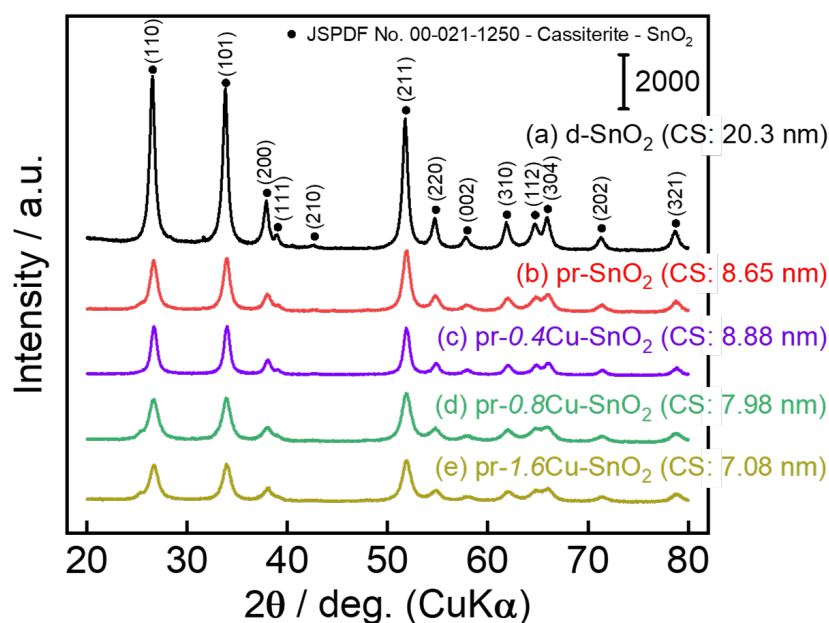


Figure 4. XRD patterns of d-SnO₂, pr-SnO₂, and pr-*w*Cu-SnO₂ (*w*: 0.4, 0.8, 1.6) powders.

Figure 5 shows the pore-size distributions of the d-SnO₂, pr-SnO₂, and pr-*w*Cu-SnO₂ (*w*: 0.4, 0.8, 1.6) powders. Most of the pores of the d-SnO₂ powder which was calculated from the N₂ desorption isotherm were observed below 20 nm, and the mixing of PMMA microspheres into the precursor solution for the ultrasonic-spray pyrolysis largely increased the pore volume as well as the pore size in the spherical SnO₂ powders. The pore size of the peaks derived from the N₂ adsorption isotherms of all the pr-*w*Cu-SnO₂ (*w*: 0.4, 0.8, 1.6) powders was larger than those derived from their N₂ desorption isotherms, whereas the pore volume of the peaks derived from the N₂ adsorption isotherms of all the powders was smaller than those derived from their N₂ desorption isotherms. Generally, the difference between pore diameters calculated from N₂ adsorption and desorption isotherms arises from the ink-bottle porous morphology of the synthesized powders. Therefore, the pore diameter calculated from the N₂ desorption isotherm reflects the width of the necks formed between the spherical pores which originate from the morphology of PMMA microspheres as a template, whereas the one calculated from N₂ adsorption isotherm reflects the diameter of the spherical pores. Actually, the size of pores on the surface of the pr-*w*Cu-SnO₂ powders (Figure 2) was quite similar to the pore diameter (ca. 30 nm) calculated from their N₂ adsorption isotherms. However, the pore diameter of the pr-SnO₂ powder calculated from N₂ adsorption isotherm (ca. 60–70 nm) is larger than that of observed by the SEM photograph (ca. 30 nm). This indicates that larger pores exist inside the pr-SnO₂ powder. The specific surface area (SSA) of the pr-SnO₂ powder (ca. 43.4 m² g⁻¹) was much larger than that of d-SnO₂ powder (ca. 9.29 m² g⁻¹). This clearly showed that the formation of porous structures inside of the spherical SnO₂ powders by using the PMMA microspheres significantly increased the SSA. The addition of Cu_xO tends to increase the SSA slightly.

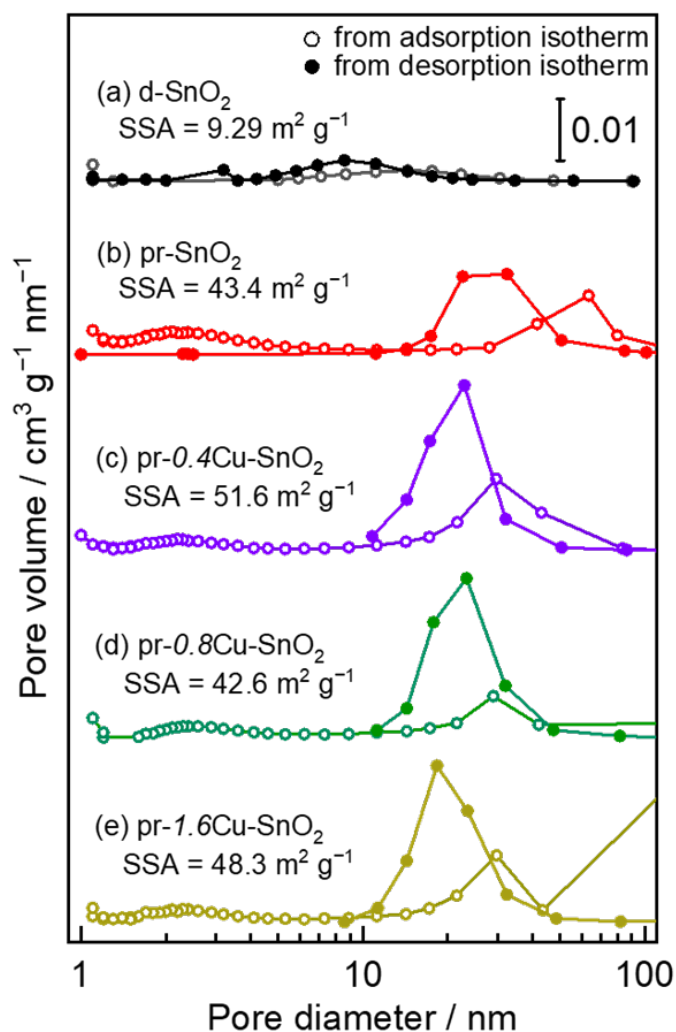


Figure 5. Pore-size distributions of as-prepared d-SnO₂, pr-SnO₂, and pr-*w*Cu-SnO₂ (*w*: 0.4, 0.8, 1.6) powders, together with their specific surface area (SSA).

Figure 6 shows representative XPS spectra of pr-SnO₂ and pr-1.6Cu-SnO₂ powders. The Sn 3d spectra were clearly assigned to the highest oxidation state of Sn (i.e., Sn⁴⁺ of SnO₂) [36,37]. However, the loading of Cu_xO onto SnO₂ negatively shifted the peak energy of the Sn 3d_{5/2} (495.5 eV to 495.3 eV) and Sn 3d_{3/2} (487.1 eV to 486.9 eV), which can be attributed to the electron transfer from Cu_xO to SnO₂ [28–40]. The O 1s spectra of the pr-SnO₂ and pr-1.6Cu-SnO₂ powders were deconvoluted into three components (531.1, 531.8, and 532.5 eV for pr-SnO₂ and 530.9, 531.8, and 532.4 eV for pr-1.6Cu-SnO₂), which originate from lattice oxygen (O²⁻), chemisorbed oxygen (O_{ads}), and hydroxyl surface groups (OH⁻), respectively [41–44]. The binding energies of the Cu components showed a major doublet of both Cu 2p_{3/2} and Cu 2p_{1/2} (ca. 932.7 eV and 952.5 eV, respectively, derived from Cu⁺ of Cu₂O), together with a minor doublet (934.6 eV (Cu 2p_{3/2}) and 954.3 eV (Cu 2p_{1/2}), derived from Cu²⁺ of CuO) [37,45]. In addition, the Cu content of the pr-1.6Cu-SnO₂ powders was estimated to be 1.68 wt%, based on the XPS results. These results indicated that Cu₂O was mainly dispersed into the pr-1.6Cu-SnO₂ powders and that the p–n junctions were formed at the interfaces between Cu₂O and SnO₂.

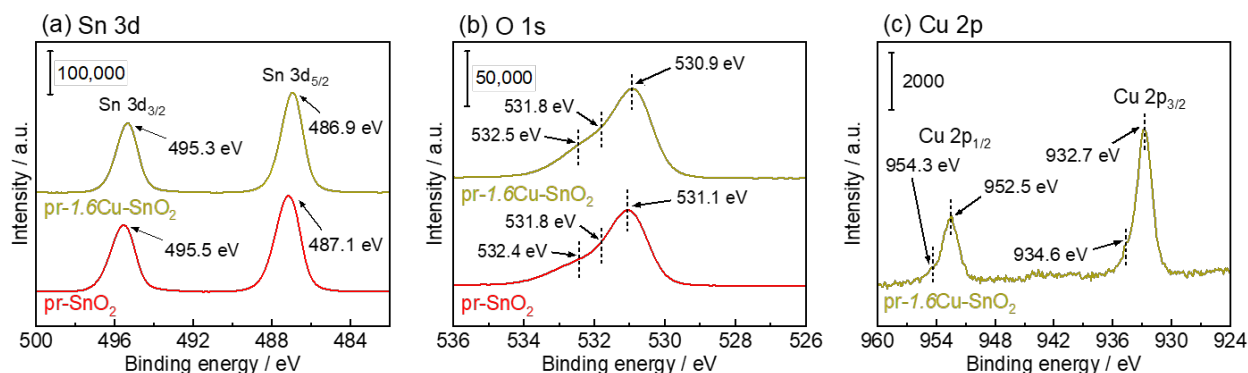


Figure 6. (a) Sn 3d, (b) O 1s, and (c) Cu 2p XPS spectra of as-prepared pr-SnO₂ and pr-1.6Cu-SnO₂ powders.

3.2. Gas-Sensing Properties

Figure 7 shows representative response transients of pr-SnO₂ and pr-1.6Cu-SnO₂ sensors to 20, 50, and 100 ppm acetone at 300 °C and 400 °C in air. Figure 8 shows temperature dependences of (a) resistances in air and responses to (b) 100 ppm acetone and (c) 100 ppm toluene of the d-SnO₂, pr-SnO₂, and pr-*w*Cu-SnO₂ sensors, together with (d) concentration dependences of responses to acetone of the pr-SnO₂ and pr-*w*Cu-SnO₂ sensors at 350 °C in air. The resistance of the pr-SnO₂ sensor in the air was much smaller than that of the d-SnO₂ sensor. Besides, the addition of Cu_xO to the pr-SnO₂ powder increased the resistance in air, and the resistance of the pr-*w*Cu-SnO₂ sensor in the air increased with an increase in the additive amount of Cu_xO, because of the formation of the p–n heterojunction between SnO₂ and the surface Cu_xO.

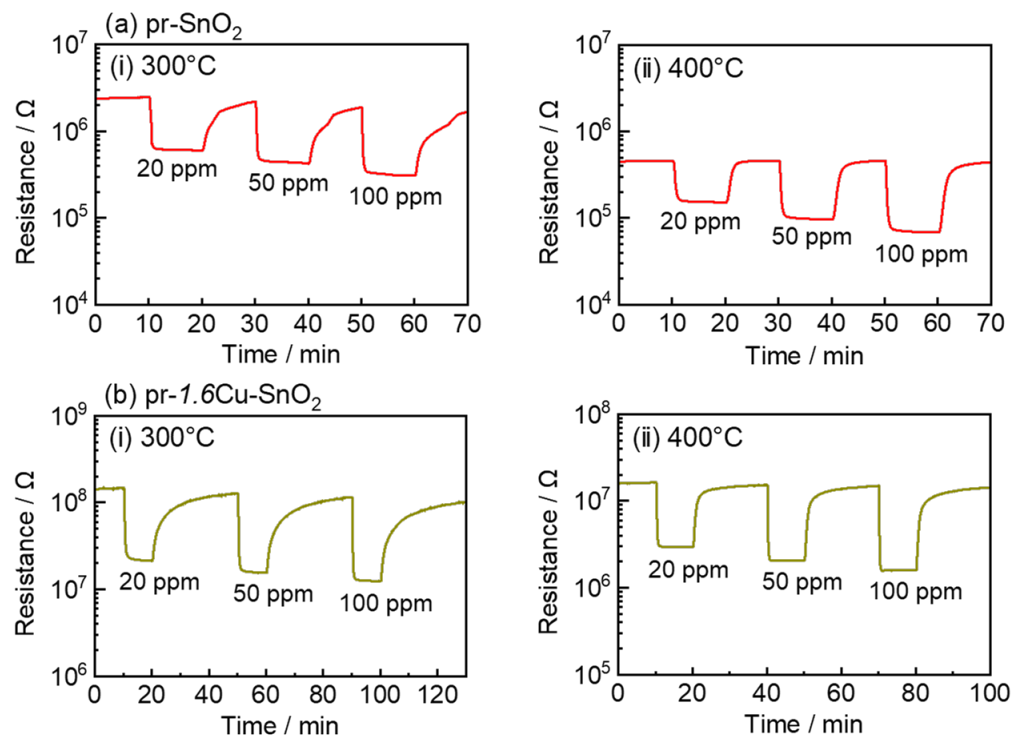


Figure 7. Response transients of (a) pr-SnO₂ and (b) pr-1.6Cu-SnO₂ sensors to 20, 50, and 100 ppm acetone at (i) 300 °C and (ii) 400 °C in air.

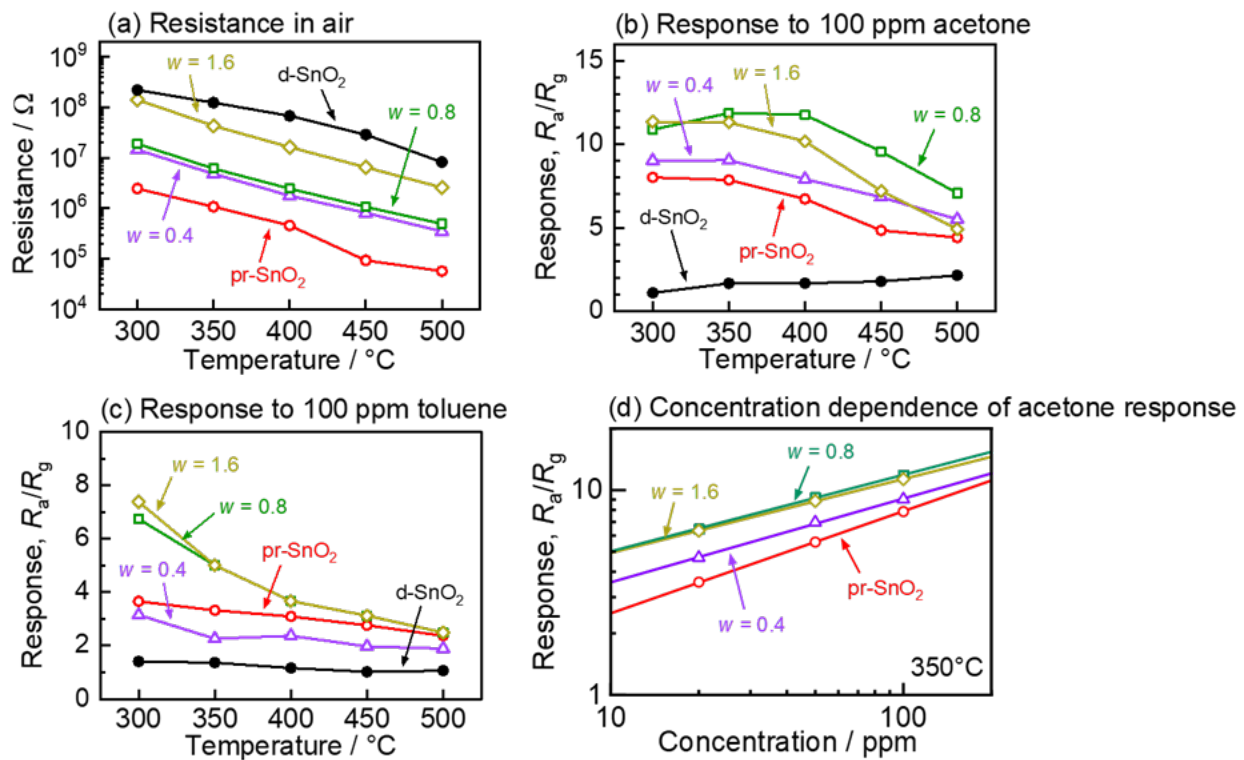


Figure 8. Temperature dependences of (a) resistances in air and responses to (b) 100 ppm acetone and (c) 100 ppm toluene of d-SnO₂, pr-SnO₂, and pr-wCu-SnO₂ sensors, together with (d) concentration dependences of responses to acetone of pr-SnO₂ and pr-wCu-SnO₂ sensors at 350 °C in air.

The resistance of all the sensors decreased upon exposure to acetone and toluene, and the resistance decreased with an increase in their concentrations. The d-SnO₂ sensor exhibited a relatively smaller response to acetone and toluene than the pr-SnO₂ sensor over the whole temperature range. The responses of all the pr-wCu-SnO₂ sensors to 100 ppm acetone were larger than that of the pr-SnO₂ sensor over the whole temperature range. The pr-0.4Cu-SnO₂ and pr-0.8Cu-SnO₂ sensors showed the largest acetone response at 350 °C. On the other hand, the acetone response of the pr-SnO₂ and the pr-1.6Cu-SnO₂ sensors monotonically decreased with increasing operating temperature. The pr-0.8Cu-SnO₂ sensor showed the largest acetone response (ca. 11.9) at 350 °C among all the sensors. The addition of 0.4 wt% Cu to pr-SnO₂ decreased the toluene response over the whole temperature range, whereas the further increase in the additive amount of Cu_xO to pr-SnO₂ improved the toluene response, especially at low temperatures. The pr-1.6Cu-SnO₂ sensor showed the largest toluene response at 300 °C. The toluene responses of all sensors at each temperature were smaller than that of the acetone responses. All the sensors showed a linear dependence between the acetone response and the logarithm of concentration (Figure 8d). The response of the pr-0.8Cu-SnO₂ sensor to 20 ppm acetone (ca. 6.24) was larger than that of the pr-SnO₂ sensor (ca. 3.55), and the slope of the response of the pr-0.8Cu-SnO₂ sensor was smaller than that of the pr-SnO₂. Therefore, the pr-0.8Cu-SnO₂ sensor seems to detect the lower concentrations of acetone. The detection limit of a sensor is commonly defined as three times the standard deviation of its noise [46–49]. According to the results obtained in this study, the detection limit of the pr-0.8Cu-SnO₂ sensor was expected to be about 158 ppb (noise: ca. 85 kΩ).

Figure 9 shows response transients to dry synthetic air (21% O₂) of the pr-SnO₂ sensor and the pr-1.6Cu-SnO₂ in dry N₂. The resistance in N₂ of both the sensors largely increased upon exposure to oxygen, which indicates that the negatively charged oxygen species adsorbed on the sensor surface in the air. In other words, there is little adsorption of negatively charged oxygen species on the sensor surface in N₂. The resistance of the pr-

SnO_2 sensor at $350\text{ }^\circ\text{C}$ in N_2 is ca. $50\text{ k}\Omega$, whereas that of the pr-1.6Cu-SnO_2 sensor is ca. $1\text{ M}\Omega$. Based on the results of STEM-EDS and XPS of the pr-1.6Cu-SnO_2 powders, it is confirmed that Cu_xO nanoparticles uniformly exist on the SnO_2 surface. Therefore, the drastic increase in the resistance by the Cu_xO addition indicates the appearance of the p–n heterojunction between SnO_2 and the surface Cu_xO . The resistance of both sensors increased with the negatively charged adsorption of oxygen. The resistances of the pr-SnO_2 and pr-1.6Cu-SnO_2 sensors increased by about 18.7 and 32.3 times, respectively. This indicates that the change in resistance becomes greater when the electron concentration in the sensor material is lower, even if the same amount of oxygen adsorbates is formed on the surface of the sensor material. Assuming that no oxygen is adsorbed on the surface in nitrogen, the magnitude of the increase in resistance of these sensors corresponds to the magnitude of their theoretical maximum responses.

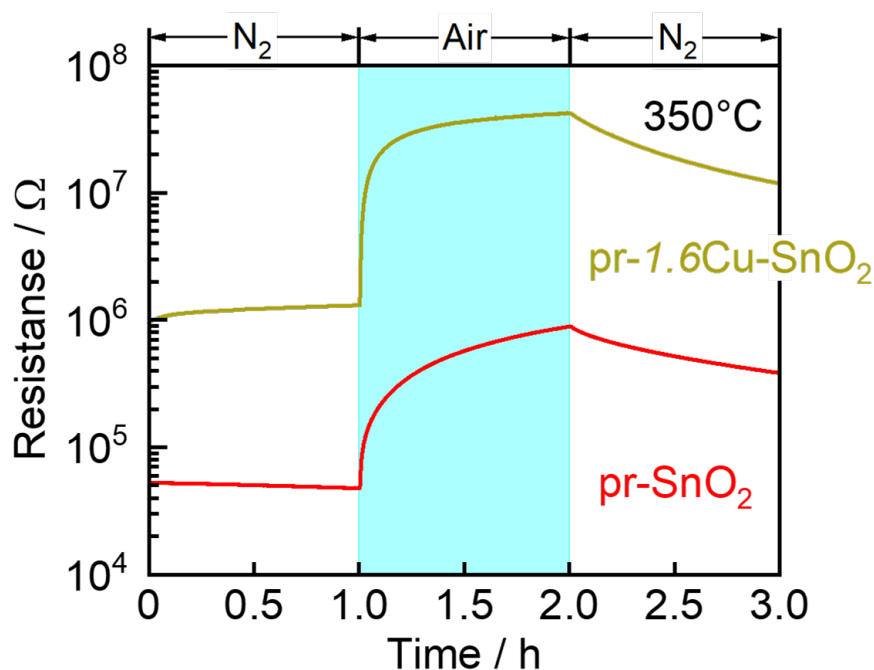


Figure 9. Response transients to dry synthetic air (21% O_2) of pr-SnO_2 and pr-1.6Cu-SnO_2 sensors in dry N_2 .

Figure 10 shows the catalytic combustion behavior of 100 ppm acetone over the pr-SnO_2 and pr-1.6Cu-SnO_2 powders in dry air. Acetone started to oxidize at $100\text{ }^\circ\text{C}$ over the pr-SnO_2 powder. Its oxidation reaction was accelerated with a rise in the temperature, and it was completely oxidized to CO_2 at $450\text{ }^\circ\text{C}$. The acetone–conversion ratio of both the powders was larger than their CO_2 -production ratio in the temperature range at the same temperatures between $100\text{ }^\circ\text{C}$ and $420\text{ }^\circ\text{C}$, which indicates that acetone was partially decomposed to be converted to some intermediates [50]. In addition, the temperature at which 50% of acetone was converted to CO_2 , T_{50} , of the pr-1.6Cu-SnO_2 powder (ca. $330\text{ }^\circ\text{C}$) was higher than that of the pr-SnO_2 powder (ca. $300\text{ }^\circ\text{C}$). In other words, the oxidation activity of acetone on the pr-1.6Cu-SnO_2 powder was smaller than that on the pr-SnO_2 powder.

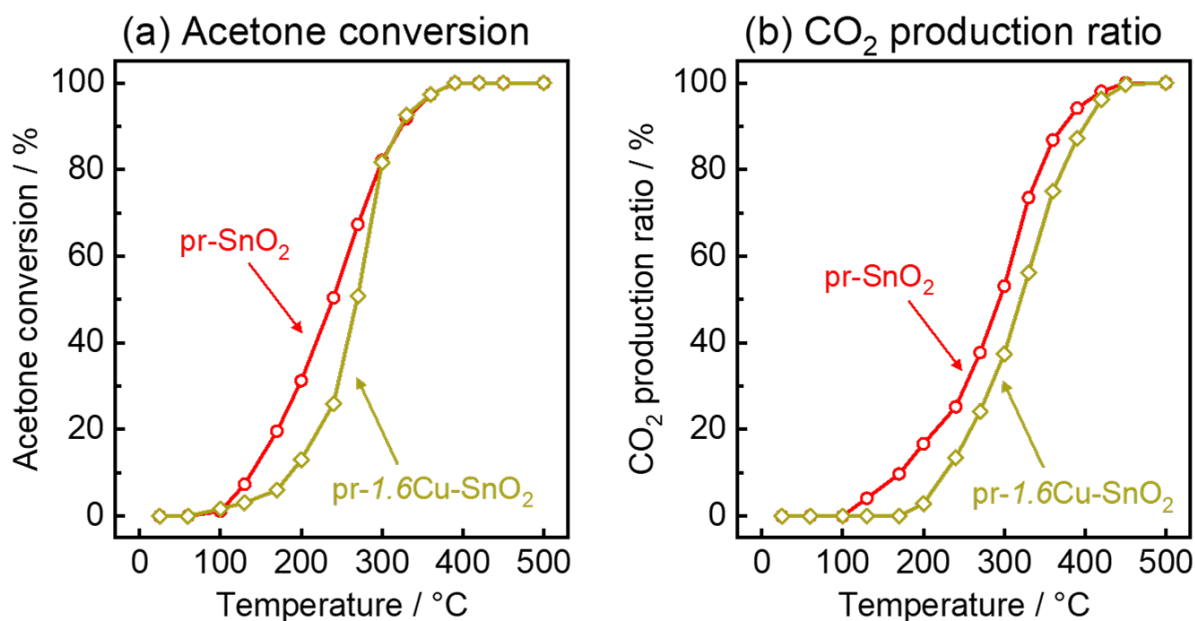


Figure 10. Catalytic combustion behavior of 100 ppm acetone over pr-SnO₂ and pr-1.6Cu-SnO₂ powders in air; (a) acetone conversion, (b) CO₂ production ratio.

Based on all the results obtained in this study, the acetone-sensing mechanism of the sensor is discussed as described below. First, the thickness of the depletion layer of the pr-SnO₂ sensor is quite thin in dry N₂, because of the small number of negatively charged oxygen adsorbates (O²⁻) on the SnO₂ surface. When the pr-SnO₂ sensor is exposed to air, the thickness of the depletion layer increases with an increase in the oxygen adsorbates to decrease the number of electrons in the bulk. The p-n heterojunction forms the depletion layer on the pr-wCu-SnO₂ surface even in dry N₂, which contributes to the further decrease in the concentration of carrier electrons. Moreover, the thickness of the depletion layer increases and the concentration of carrier electrons decreases with an increase in the amount of oxygen concentration in the base gas. Since the concentration of carrier electrons of the pr-wCu-SnO₂ sensor is much lower than that of the pr-SnO₂ sensor, the resistance of the pr-wCu-SnO₂ sensor is quite sensitive to a change in the concentration of carrier electrons (i.e., the amount of reaction of oxygen adsorbates with target gases) than that of the pr-SnO₂ sensor. This is one of the reasons why the response of the pr-wCu-SnO₂ sensor is larger than that of the pr-SnO₂ sensor. This effect of the p-n heterojunction increases with an increase in the amount of Cu components loaded onto the pr-SnO₂.

Second, the catalytic activity of acetone oxidation of the pr-wCu-SnO₂ sensor is smaller than that of the pr-SnO₂ sensor, as shown in Figure 10. While acetone diffuses in the pr-SnO₂ and pr-wCu-SnO₂ films (film thickness: ca. 15 μm), acetone is oxidized on the surface of these oxide particles. Therefore, the concentration of acetone in the innermost region of the pr-wCu-SnO₂ films is higher than that of the pr-SnO₂ film. Thus, the amount of reaction of oxygen adsorbates with acetone on the pr-wCu-SnO₂ surface is anticipated to be larger than that on the pr-SnO₂ surface. This is the second reason why the response of the pr-wCu-SnO₂ sensor is larger than that of the pr-SnO₂ sensor. The catalytic effect also increases with an increase in the additive amount of Cu_xO components loaded onto the pr-SnO₂.

Considering that the microstructure of the pr-wCu-SnO₂ powders is comparable to that of the pr-SnO₂ powder, the results obtained in this study show that the adequate control of both the formation of the p-n heterojunction (increase in the resistance) and the decrease in the catalytic activity by the loading of Cu_xO components onto the pr-SnO₂ are essential in improving the VOC-sensing properties of the pr-SnO₂ sensor.

4. Conclusions

Spherical pr-SnO₂ and pr-wCu-SnO₂ powders were prepared by ultrasonic spray pyrolysis using SnCl₄ and CuCl₂ aqueous solutions containing PMMA microspheres as a template. All the powders were confirmed to show a porous structure formed by the thermal decomposition of PMMA microspheres. The pr-0.8Cu-SnO₂ sensor showed the largest acetone response at 350 °C among all the sensors. In addition, pr-wCu-SnO₂ (w: 0.4, 0.8, 1.6) sensors showed linear dependences between the acetone response and the logarithm of the concentration, and the slope of the response of the pr-0.8Cu-SnO₂ sensor was smaller than that of the pr-SnO₂. Therefore, the pr-0.8Cu-SnO₂ sensor seems to detect the lower concentrations of acetone. The resistance of the pr-1.6Cu-SnO₂ sensor in dry N₂ was much larger than that of the pr-SnO₂ sensor, due to the formation of the p-n heterojunction between SnO₂ and Cu_xO, and the resistance of the pr-1.6Cu-SnO₂ sensor largely increased upon exposure to dry air in comparison with that of the pr-SnO₂ sensor. Therefore, the addition of Cu_xO to the pr-SnO₂ powder increased the theoretical maximum response. In addition, the oxidation activity of acetone on the pr-1.6Cu-SnO₂ surface was smaller than that on the pr-SnO₂ surface, which indicates that the concentration of acetone in the innermost region of the pr-1.6Cu-SnO₂ film was higher than that of the pr-SnO₂ film. This is another reason for the relatively large response of the pr-1.6Cu-SnO₂ sensor.

Author Contributions: Conceptualization, S.T. and T.U.; investigation, S.T., T.U. and K.K.; writing—original draft preparation, S.T.; writing—review and editing, T.H.; supervision, T.H. and Y.S.; funding acquisition, T.U., T.H. and Y.S. All authors have read and agreed to the published version of the manuscript.

Funding: This research received no external funding.

Institutional Review Board Statement: Not applicable.

Informed Consent Statement: Not applicable.

Data Availability Statement: The data that support the findings of this study are available from the corresponding author upon reasonable request.

Acknowledgments: This study was supported, in part, by the Nagasaki University WISE Programme Research Grant for Global Health Research.

Conflicts of Interest: The authors declare no conflict of interest.

References

1. Mølhave, L.; Clausen, G.; Berglund, B.; Ceaurriz, J.; Kettrup, A.; Lindvall, T.; Maroni, M.; Pickering, A.C.; Risse, U.; Rothweiler, H.; et al. Total Volatile Organic Compounds (TVOC) in Indoor Air Quality Investigations. *Indoor Air* **1997**, *7*, 225–240. [[CrossRef](#)]
2. Gong, Y.; Wei, Y.; Cheng, J.; Jiang, T.; Chen, L.; Xu, B. Health risk assessment and personal exposure to Volatile Organic Compounds (VOCs) in metro carriages—A case study in Shanghai, China. *Sci. Total Environ.* **2017**, *574*, 1432–1438. [[CrossRef](#)] [[PubMed](#)]
3. Haick, H.; Broza, Y.Y.; Mochalski, P.; Ruzsanyi, V.; Amann, A. Assessment, origin, and implementation of breath volatile cancer markers. *Chem. Soc. Rev.* **2014**, *43*, 1423–1449. [[CrossRef](#)] [[PubMed](#)]
4. Koo, W.-T.; Choi, S.-J.; Kim, N.-H.; Jang, J.-S.; Kim, I.-D. Catalyst-decorated hollow WO₃ nanotubes using layer-by-layer self-assembly on polymeric nanofiber templates and their application in exhaled breath sensor. *Sens. Actuators B* **2016**, *223*, 301–310. [[CrossRef](#)]
5. Yaegaki, K.; Sanada, K. Volatile sulfur compounds in mouth air from clinically healthy subjects and patients with periodontal disease. *J. Periodont. Res.* **1992**, *27*, 233–238. [[CrossRef](#)] [[PubMed](#)]
6. Kalidoss, R.; Umopathy, S. An overview on the exponential growth of non-invasive diagnosis of diabetes mellitus from exhaled breath by nanostructured metal oxide Chemi-resistive gas sensors and μ-preconcentrator. *Biomed. Microdev.* **2020**, *22*, 2–9. [[CrossRef](#)]
7. Li, W.; Dai, W.; Liu, M.; Long, Y.; Wang, C.; Xie, S.; Liu, Y.; Zhang, Y.; Shi, Q.; Peng, X.; et al. VOC biomarkers identification and predictive model construction for lung cancer based on exhaled breath analysis: Research protocol for an exploratory study. *BMJ Open* **2019**, *9*, e028448. [[CrossRef](#)]
8. Peng, G.; Tisch, U.; Adams, O.; Hakim, M.; Shehada, N.; Broza, Y.Y.; Billan, S.; Bortnyak, R.A.; Kuten, A.; Haick, H. Diagnosing lung cancer in exhaled breath using gold nanoparticles. *Nat. Nanotechnol.* **2009**, *4*, 669–673. [[CrossRef](#)] [[PubMed](#)]

9. Amann, A.; Corradi, M.; Mazzone, P.; Mutti, A. Lung cancer biomarkers in exhaled breath. *Expert Rev. Mol. Diagn.* **2011**, *11*, 207–217. [[CrossRef](#)]
10. Shin, J.; Choi, S.-J.; Lee, I.; Youn, D.-Y.; Park, C.O.; Lee, J.-H.; Tuller, H.L.; Kim, I.-D. Thin-wall assembled SnO₂ fibers functionalized by catalytic Pt nanoparticles and their superior exhaled-breath-sensing properties for the diagnosis of diabetes. *Adv. Funct. Mater.* **2013**, *23*, 2357–2367. [[CrossRef](#)]
11. Hieda, K.; Hyodo, T.; Shimizu, Y.; Egashira, M. Preparation of porous tin dioxide powder by ultrasonic spray pyrolysis and their application to sensor materials. *Sens. Actuators B* **2008**, *133*, 144–150. [[CrossRef](#)]
12. Hyodo, T.; Iwanaga, A.; Ishida, K.; Kamada, K.; Ueda, T.; Shimizu, Y. Effects of noble-metal loading and ultraviolet-light irradiation on gas sensing properties of porous indium oxide films at room temperature. *J. Ceram. Soc. Jpn.* **2021**, *129*, 676–682. [[CrossRef](#)]
13. Hyodo, T.; Fujii, E.; Ishida, K.; Ueda, T.; Shimizu, Y. Microstructural control of porous In₂O₃ powders prepared by ultrasonic-spray pyrolysis employing self-synthesized polymethylmethacrylate microspheres as a template and their NO₂-sensing properties. *Sens. Actuators B* **2017**, *244*, 992–1003. [[CrossRef](#)]
14. Hyodo, T.; Furuno, S.; Fujii, E.; Matsuo, K.; Motokucho, S.; Kojio, K.; Shimizu, Y. Porous In₂O₃ powders prepared by ultrasonic-spray pyrolysis as a NO₂-sensing material: Utilization of polymethylmethacrylate microspheres synthesized by ultrasonic-assisted emulsion polymerization as a template. *Sens. Actuators B* **2013**, *187*, 495–502. [[CrossRef](#)]
15. Ueda, T.; Boehme, I.; Hyodo, T.; Shimizu, Y.; Weimar, U.; Barsan, N. Effects of gas adsorption properties of an Au-loaded porous In₂O₃ sensor on NO₂-sensing properties. *ACS Sens.* **2021**, *6*, 4019–4026. [[CrossRef](#)] [[PubMed](#)]
16. Ueda, T.; Boehme, I.; Hyodo, T.; Shimizu, Y.; Weimar, U.; Barsan, N. Enhanced NO₂-sensing properties of Au-loaded porous In₂O₃ gas sensors at low operating temperatures. *Chemosensors* **2020**, *8*, 72. [[CrossRef](#)]
17. Ueda, T.; Ishida, K.; Kamada, K.; Hyodo, T.; Shimizu, Y. Improvement in NO₂ sensing properties of semiconductor-type gas sensors by loading of Au into porous In₂O₃ powders. *Front. Mater.* **2019**, *6*, 81. [[CrossRef](#)]
18. Sang, L.; Xu, G.; Chen, Z.; Wang, X.; Cui, H.; Zhang, G.; Dou, Y. Synthesis and characterization of Au-loaded SnO₂ mesoporous spheres by spray drying and their gas sensing property. *Mater. Sci. Semicond. Process.* **2020**, *105*, 104710. [[CrossRef](#)]
19. Liu, Y.; Li, X.; Wang, Y.; Li, X.; Cheng, P.; Zhao, Y.; Dang, F.; Zhang, Y. Hydrothermal synthesis of Au@SnO₂ hierarchical hollow microspheres for ethanol detection. *Sens. Actuators B Chem.* **2020**, *319*, 128299. [[CrossRef](#)]
20. Bouchikhi, B.; Chludziński, T.; Saidi, T.; Smulko, J.; Bari, N.E.; Wen, H.; Ionescu, R. Formaldehyde detection with chemical gas sensors based on WO₃ nanowires decorated with metal nanoparticles under dark conditions and UV light irradiation. *Sens. Actuators B Chem.* **2020**, *320*, 128331. [[CrossRef](#)]
21. Zeb, S.; Sun, G.; Nie, Y.; Cui, Y.; Jiang, X. Synthesis of highly oriented WO₃ nanowire bundles decorated with Au for gas sensing application. *Sens. Actuators B Chem.* **2020**, *321*, 128439. [[CrossRef](#)]
22. Lian, X.; Li, Y.; Zhu, J.; An, D.; Wang, Q. Fabrication of Au-decorated SnO₂ nanoparticles with enhanced n-butanol gas sensing properties. *Mater. Sci. Semicond. Process.* **2019**, *101*, 198–205. [[CrossRef](#)]
23. Tammanoon, N.; Iwamoto, T.; Ueda, T.; Hyodo, T.; Wisitorsaat, A.; Liewhiran, C.; Shimizu, Y. Synergistic effects of PdOx-CuOx loadings on methylmercaptan sensing of porous WO₃ microspheres prepared by ultrasonic spray pyrolysis. *ACS Appl. Mater. Interfaces* **2020**, *12*, 41728–41739. [[CrossRef](#)] [[PubMed](#)]
24. Staerz, A.; Kim, T.-H.; Lee, J.-H.; Weimar, U.; Barsan, N. Nanolevel control of gas sensing characteristics via p–n heterojunction between Rh₂O₃ Clusters and WO₃ crystallites. *J. Phys. Chem. C* **2017**, *121*, 24701–24706. [[CrossRef](#)]
25. Jayababu, N.; Poloju, M.; Shruthi, J.; Reddy, M.V.R. Semi shield driven p-n heterostructures and their role in enhancing the room temperature ethanol gas sensing performance of NiO/SnO₂ nanocomposites. *Ceram. Int.* **2019**, *45*, 15134–15142. [[CrossRef](#)]
26. Cai, Z.; Park, S. Enhancement mechanisms of ethanol-sensing properties based on Cr₂O₃ nanoparticle-anchored SnO₂ nanowires. *J. Mater. Res. Technol.* **2020**, *9*, 271–281. [[CrossRef](#)]
27. Kim, H.; Cai, Z.; Chang, S.P.; Park, S. Improved sub-ppm acetone sensing properties of SnO₂ nanowire-based sensor by attachment of Co₃O₄ nanoparticles. *J. Mater. Res. Technol.* **2020**, *9*, 1129–1136. [[CrossRef](#)]
28. Xu, Y.; Zheng, L.; Yang, C.; Liu, X.; Zhang, J. Highly sensitive and selective electronic sensor based on Co catalyzed SnO₂ nanospheres for acetone detection. *Sens. Actuators B Chem.* **2020**, *304*, 127237. [[CrossRef](#)]
29. Kou, X.; Xie, N.; Chen, F.; Wang, T.; Guo, L.; Wang, C.; Wang, Q.; Ma, J.; Sun, Y.; Zhang, H.; et al. Superior acetone gas sensor based on electrospun SnO₂ nanofibers by Rh doping. *Sens. Actuators B Chem.* **2018**, *256*, 861–869. [[CrossRef](#)]
30. Gu, C.; Cui, Y.; Wang, L.; Sheng, E.; Shim, J.J.; Huang, J. Synthesis of the porous NiO/SnO₂ microspheres and microcubes and their enhanced formaldehyde gas sensing performance. *Sens. Actuators B Chem.* **2017**, *241*, 298–307. [[CrossRef](#)]
31. Gschwend, P.M.; Schenk, F.M.; Gogos, A.; Prasinis, S.E. Acetone sensing and catalytic conversion by Pd-loaded SnO₂. *Materials* **2021**, *14*, 5921. [[CrossRef](#)] [[PubMed](#)]
32. Güntner, A.T.; Weber, I.C.; Prasinis, S.E. Catalytic filter for continuous and selective ethanol removal prior to gas sensing. *ACS Sens.* **2020**, *5*, 1058–1067. [[CrossRef](#)]
33. Weber, I.C.; Braun, H.P.; Krumeich, F.; Güntner, A.T.; Prasinis, S.E. Superior acetone selectivity in gas mixtures by catalyst-filtered chemoresistive sensors. *Adv. Sci.* **2020**, *7*, 20001503. [[CrossRef](#)]
34. Kato, T.; Tashiro, M.; Sugimura, K.; Hyodo, T.; Shimizu, Y.; Egashira, M. Preparation of hollow alumina microspheres by ultrasonic spray pyrolysis. *J. Ceram. Soc. Jpn.* **2002**, *110*, 146–148. [[CrossRef](#)]

35. Hyodo, T.; Inoue, H.; Motomura, H.; Matsuo, K.; Hashishin, T.; Tamaki, J.; Shimizu, Y.; Egashira, M. NO₂ sensing properties of macroporous In₂O₃-based powders fabricated by utilizing ultrasonic spray pyrolysis employing polymethylmethacrylate microspheres as a template. *Sens. Actuators B Chem.* **2010**, *151*, 265–273. [[CrossRef](#)]
36. Costa, I.M.; Colmenares, Y.N.; Pizani, P.S.; Leite, E.R.; Chiquito, A.J. Sb doping of VLS synthesized SnO₂ nanowires probed by Raman and XPS spectroscopy. *Chem. Phys. Lett.* **2018**, *695*, 125–130. [[CrossRef](#)]
37. Choi, K.-I.; Kim, H.-J.; Kang, Y.C.; Lee, J.-H. Ultrasensitive and ultrasensitive detection of H₂S in highly humid atmosphere using CuO-loaded SnO₂ hollow spheres for real-time diagnosis of halitosis. *Sens. Actuators B Chem.* **2014**, *194*, 371–376. [[CrossRef](#)]
38. Kim, J.-S.; Na, C.W.; Kwak, C.-H.; Li, H.-Y.; Yoon, J.W.; Kim, J.-H.; Jeong, S.-Y.; Lee, J.-H. Humidity-Independent gas sensors using Pr-doped In₂O₃ macroporous spheres: Role of cyclic Pr³⁺/Pr⁴⁺ redox reactions in suppression of water-poisoning effect. *ACS Appl. Mater. Interfaces* **2019**, *11*, 25322–25329. [[CrossRef](#)] [[PubMed](#)]
39. Du, N.; Zhang, H.; Chen, B.D.; Ma, X.Y.; Liu, Z.H.; Wu, J.B.; Yang, Y.R. Porous indium oxide nanotubes: Layer-by-layer assembly on carbon-nanotube templates and application for room-temperature NH₃ gas sensors. *Adv. Mater.* **2017**, *19*, 1641–1645. [[CrossRef](#)]
40. Sun, Y.; Zhao, Z.; Suematsu, K.; Li, P.; Yu, Z.; Zhang, W.; Hu, J.; Shimano, K. Rapid and stable detection of carbon monoxide in changing humidity atmospheres using clustered In₂O₃/CuO Nanospheres. *ACS Sens.* **2020**, *4*, 1040–1049. [[CrossRef](#)] [[PubMed](#)]
41. Sun, L.; Liu, X.; Liu, K.; Yin, S.; Chen, Q.L.; Kuang, Q.; Han, X.G.; Xie, Z.X.; Wang, C. Template-free construction of hollow α-Fe₂O₃ hexagonal nanocolumn particles with an exposed special surface for advanced gas sensing properties. *Nanoscale* **2015**, *21*, 9416–9420. [[CrossRef](#)]
42. Mao, Y.Z.; Ma, S.; Li, X.B.; Wang, C.Y.; Li, F.M. Effect of Mn doping on the microstructures and sensing properties of ZnO nanofibers. *Appl. Surf. Sci.* **2014**, *298*, 109–115. [[CrossRef](#)]
43. Gonzalez-Elipe, A.R.; Espinos, J.P.; Fernandez, A.; Munuera, G. XPS study of the surface carbonation/hydroxylation state of metal oxides. *Appl. Surf. Sci.* **1990**, *45*, 103–108. [[CrossRef](#)]
44. Wang, L.; Ma, S.; Xu, X.; Li, J.; Yang, T.; Cao, P.; Yun, P.; Wang, S.; Han, T. Oxygen vacancy-based Tb-doped SnO₂ nanotubes as an ultra-sensitive sensor for ethanol detection. *Sens. Actuators B Chem.* **2021**, *344*, 130111. [[CrossRef](#)]
45. Poulston, S.; Parlett, P.M.; Stone, P.; Bowker, M. Surface oxidation and reduction of CuO and Cu₂O studied using XPS and XAES. *Surf. Interface Anal.* **1996**, *24*, 811–820. [[CrossRef](#)]
46. Sun, J.; Sun, L.; Han, N.; Chu, H.; Bai, S.; Shu, X.; Luo, R.; Chen, A. rGO decorated CdS/CdO composite for detection of low concentration NO₂. *Sens. Actuators B Chem.* **2019**, *299*, 126832. [[CrossRef](#)]
47. Mahdavi, A.; Navaei, M.; Hesketh, P.J.; Findlay, M.; Stetter, J.R.; Hunter, W.G. Transient thermal response of micro-thermal conductivity detector (μTCD) for the identification of gas mixtures: An ultra-fast and low power method. *Microsyst. Nanoeng.* **2015**, *1*, 15025. [[CrossRef](#)]
48. Struk, D.; Shirke, A.; Mahdavi, A.; Hesketh, P.J.; Stetter, J.R. Investigating time-resolved response of micro thermal conductivity sensor under various modes of operation. *Sens. Actuators B Chem.* **2018**, *254*, 771–777. [[CrossRef](#)]
49. Jung, G.; Shin, W.; Hong, S.; Jeong, Y.; Park, J.; Kim, D.; Bae, J.H.; Park, B.G.; Lee, J.H. Comparison of the characteristics of semiconductor gas sensors with different transducers fabricated on the same substrate. *Sens. Actuators B Chem.* **2021**, *335*, 129661. [[CrossRef](#)]
50. Bianchi, C.L.; Gatto, S.; Pirola, C.; Naldoni, A.; Di Michele, A.; Cerrato, G.; Crocellà, V.; Capucci, V. Photocatalytic degradation of acetone, acetaldehyde and toluene in gas-phase: Comparison between nano and micro-sized TiO₂. *Appl. Catal. B Environ.* **2014**, *146*, 123–130. [[CrossRef](#)]

Disclaimer/Publisher’s Note: The statements, opinions and data contained in all publications are solely those of the individual author(s) and contributor(s) and not of MDPI and/or the editor(s). MDPI and/or the editor(s) disclaim responsibility for any injury to people or property resulting from any ideas, methods, instructions or products referred to in the content.